Journal of Electronic Materials
https://doi.org/10.1007/s11664-026-13088-2

ORIGINAL RESEARCH ARTICLE

Effect of Al_2O_3 Content on the High-Frequency Magnetic Properties of Fe-Si Soft Magnetic Composites Prepared by SPS

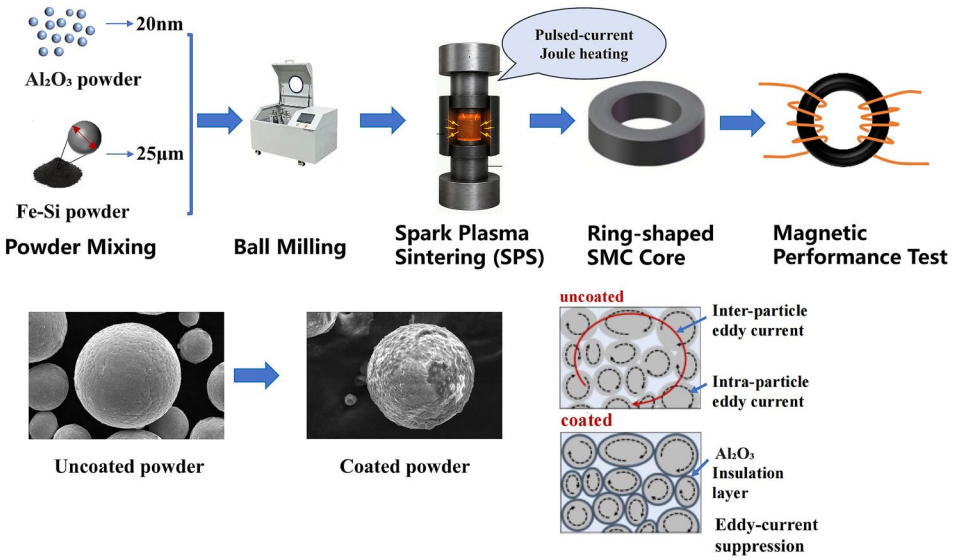
Fugui Liu[1] · Yupeng Chen[1] · Changgeng Zhang[1] · Zhiwei Lin[1,2] · Yongjian Li[1] · Kai Liu[1]

Received: 22 May 2026 / Accepted: 20 July 2026
© The Minerals, Metals & Materials Society 2026

Abstract

Fe-Si soft magnetic composites (SMCs) typically suffer from deteriorated permeability stability and increased eddy-current loss under high-frequency operating conditions, which limits their application in advanced power electronics. In this work, Fe−6.5 wt.% Si SMCs coated with Al_2O_3 insulating layers were fabricated by high-energy ball milling followed by spark plasma sintering (SPS). The influence of Al_2O_3 content on the microstructure, electrical resistivity, and magnetic properties was systematically investigated over a frequency range below 500 kHz. The results show that the introduction of Al_2O_3 effectively enhances the electrical insulation between Fe-Si particles, leading to increased resistivity and reduced high-frequency core loss. Scanning electron microscopy (SEM) and energy-dispersive x-ray spectroscopy (EDS) line-scan results indicate that, as the Al_2O_3 content increases from 2.5 wt.% to 7.5 wt.%, the coating layer on the surface of Fe-Si particles evolves from incomplete coverage to a more continuous Al_2O_3 insulating coverage. This structural evolution is accompanied by improved permeability stability and a substantial reduction in magnetic loss. Among the investigated samples, the SMC containing 7.5 wt.% Al_2O_3 achieves the most favorable balance between permeability stability and core-loss reduction. The improved magnetic properties are mainly attributed to the enhanced interparticle insulation and the suppression of eddy-current effects provided by the Al_2O_3 coating. These results provide useful insights into the optimization of Fe-Si soft magnetic composites for high-frequency applications.

Graphical Abstract



Keywords Soft magnetic composites · spark plasma sintering · eddy current loss suppression · magnetic loss analysis

Extended author information available on the last page of the article

Published online: 05 August 2026

Introduction

With the development of modern electronic information technology and the rapid upgrading of communication equipment, electronic devices are moving towards miniaturization and integration.[1] This trend requires magnetic materials to exhibit not only excellent electromagnetic performance but also compatibility with miniaturized and lightweight electronic devices,[2] which poses substantial challenges for the development of advanced magnetic materials. However, the emergence and rapid development of soft magnetic composites (SMCs)[3] have provided an effective solution to the aforementioned issues.

Fe-Si soft magnetic composites are highly favored due to their high saturation magnetization, excellent DC bias performance, and cost-effectiveness. They are widely used in high-current and high-power electronic devices, such as the iron cores of filters and reactors.[4–8] Nevertheless, Fe-Si SMCs suffer from rapid permeability degradation and a sharp increase in eddy-current loss under high-frequency operating conditions, leading to the attenuation of energy conversion efficiency.[9] Applying an insulating coating on the surface of the powder matrix to restrict the interparticle eddy-current effect is a primary approach to reducing loss.[10,11]

The insulating coatings for SMCs include phosphate coating,[12,13] metal oxide coating (including MgO, Al_2O_3, and Fe_2O_3),[14] and ferrite coating (including Ni-Zn and Mn-Zn ferrites).[15] Among these, Al_2O_3 is one of the preferred materials for inorganic insulating layers, as it exhibits simple preparation, high resistivity, good thermal stability, and relatively high thermal conductivity. Li et al.[16] obtained an Al_2O_3 insulating layer on the surface of flake-shaped FeSiAl via nitric acid passivation, resulting in SMCs with low loss and high permeability at high frequencies. Zheng et al.[17] prepared Fe SMCs with an Al_2O_3 insulating layer based on the hydrolysis principle of aluminum nitrate, which effectively achieved stable permeability in the range of 5-300 kHz and low loss in the range of 5-100 kHz. Yaghtin et al.[18] fabricated a uniform Al_2O_3 coating on the surface of iron powder using the sol-gel method, and the frequency stability of the magnetic properties of the SMCs was significantly improved.

Spark plasma sintering (SPS) is an advanced powder consolidation technique that integrates pulsed electric current and uniaxial pressure to achieve rapid densification in a relatively short processing period.[19] Compared with the conventional process of cold compaction combined with annealing, SPS offers significantly higher heating rates and shorter holding times. This advantage helps to limit excessive grain growth and avoid prolonged thermal exposure of the materials, thus reducing structural defects. Additionally, the high densification achieved by SPS can effectively reduce structural flaws such as pores and weak interparticle bonding, further enhancing the structural integrity and magnetic properties of soft magnetic composites (SMCs).[20] Therefore, SPS serves as an effective processing method for fabricating Fe-Si-based SMCs with high density and reduced structural defects.

Although Al_2O_3 coatings have been reported to improve the magnetic performance of Fe-based soft magnetic composites, the effect of Al_2O_3 content on the coating structure and magnetic properties of Fe-Si SMCs still requires further investigation. In particular, the relationship between the evolution of the insulating layer on Fe-Si particle surfaces and the improvement in electrical resistivity, permeability stability, and high-frequency loss has not been fully clarified. Therefore, it is necessary to systematically investigate the influence of Al_2O_3 content on the microstructure and magnetic performance of Fe-Si SMCs.

In this work, Fe−6.5 wt.% Si/Al_2O_3 soft magnetic composites were prepared by high-energy ball milling combined with SPS. The influence of Al_2O_3 content on the microstructure, electrical resistivity, permeability, and core-loss behavior was systematically investigated. The results indicate that an appropriate Al_2O_3 content effectively improves the interparticle insulation and high-frequency magnetic performance of Fe-Si SMCs. As the Al_2O_3 content increases from 2.5 wt.% to 7.5 wt.%, the insulating layer on the surface of Fe-Si particles gradually evolves from incomplete coverage to a more continuous Al_2O_3-rich insulating coverage. Among the investigated samples, the composite containing 7.5 wt.% Al_2O_3 exhibits a favorable balance between permeability retention and core-loss reduction.

Experimental

Preparation of Fe−6.5 wt.% Si/Al_2O_3 SMCs

Fe−6.5 wt.% Si powders and nano-Al_2O_3 were both commercially sourced materials. The Fe−6.5 wt.% Si powder, with an average particle size of 25 μm, was purchased from Hunan Fushel Technology Co., Ltd., while the nano-Al_2O_3 powder, with an average particle size of 20 nm, was obtained from Shanghai Macklin. The preparation of Fe−6.5 wt.% Si/Al_2O_3 SMCs consisted of the following steps. First, a planetary ball mill was employed to introduce Al_2O_3 coating layers onto the surface of Fe-Si powders through a high-energy ball-milling process, thereby producing coated powders. The ball-milling duration was 2 h at a rotational speed of 500 r/min. Fe−6.5 wt.% Si powders were mixed with Al_2O_3 at mass fractions of 0.0 wt.%, 2.5 wt.%, 5.0 wt.%, 7.5 wt.%, and 10.0 wt.%, respectively, prior to high-energy milling.

Subsequently, the composite powders were consolidated into SMCs using SPS. The SMCs were toroidal cores with an outer diameter of 30 mm, an inner diameter of 16 mm, and a height of 5 mm. The SPS process was conducted under a uniaxial pressure of 200 MPa and a heating rate of 20°C/min. The temperature was increased to 500°C, held for 10 min, and then allowed to cool naturally to room temperature.

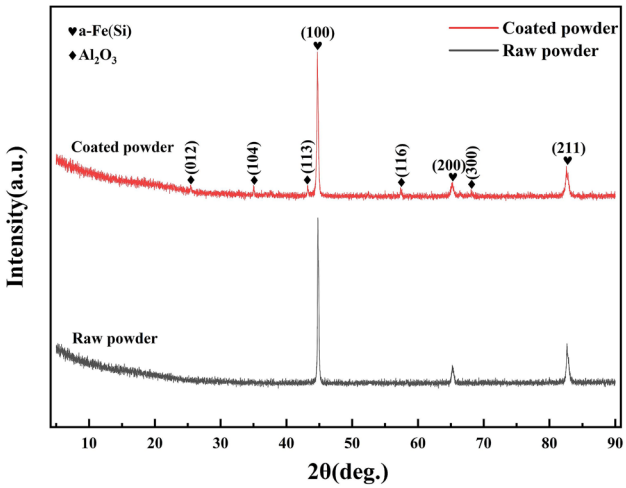


Fig. 1 XRD patterns of Fe-Si powders with and without Al_2O_3 addition.

Characterization

The morphology and microstructure of the composite powders and soft magnetic composites (SMCs) were observed using a scanning electron microscope (SEM, Nova 400 model, FEI, USA) equipped with an energy-dispersive x-ray spectrometer (EDS). The quasi-static B-H loops of the SMC samples were measured using a vibrating sample magnetometer (VSM, Quantum Design). The core loss and relative permeability of the SMCs were determined at an applied induction of 20 mT using a hysteresis loop automatic tester (AMH-1 M-S model). The electrical resistivity of the SMCs was measured using the four-point probe method.[21] All tests were performed at room temperature, and the sample density was calculated based on the Archimedes principle.

Results and Discussion

Microstructures of Fe-Si/Al_2O_3 Core-Shell Powders

As shown in Fig. 1, the x-ray diffraction (XRD) pattern of the pristine Fe-Si powder exhibits three strong characteristic diffraction peaks corresponding to the α-Fe(Si) phase with a body-centered cubic (BCC) structure. For the uncoated Fe-Si powder, the three peak positions are located at 44.87° (110), 65.46° (200), and 82.87° (211), respectively. After the introduction of nano-Al_2O_3, the

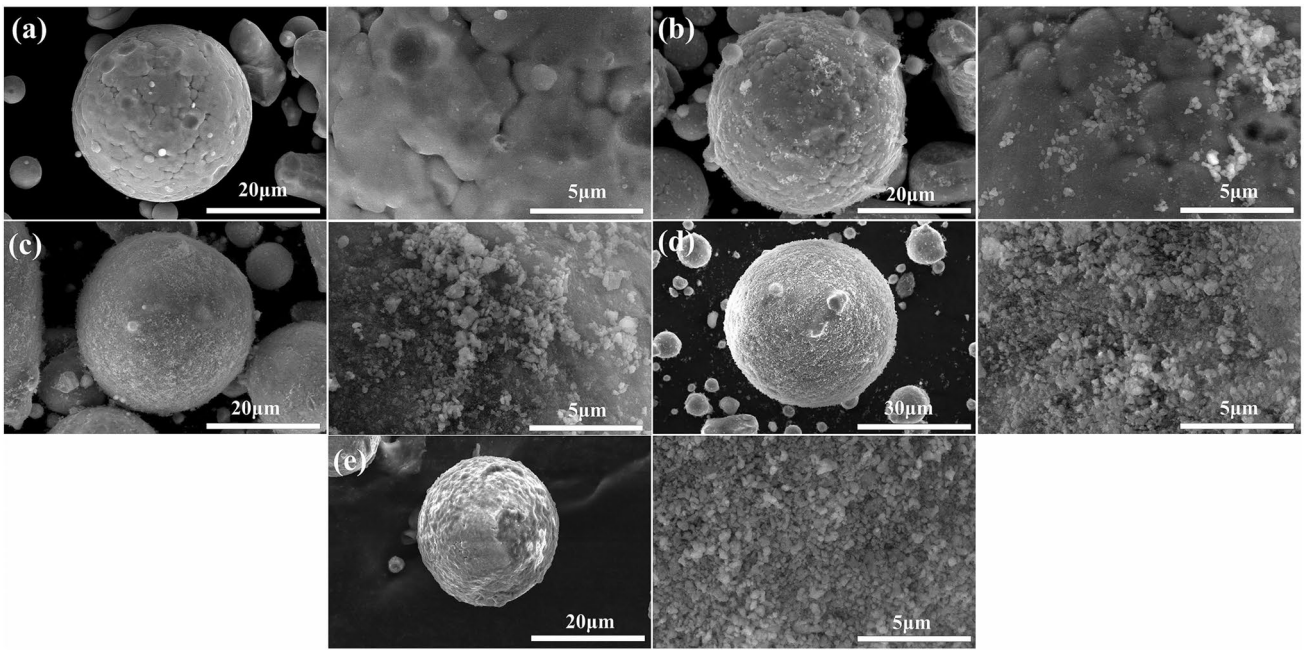


Fig. 2 SEM images and magnified local surface morphologies of Fe-Si particles with various Al_2O_3 contents: (a) 0.0 wt.%, (b) 2.5 wt.%, (c) 5.0 wt.%, (d) 7.5 wt.%, and (e) 10.0 wt.%.

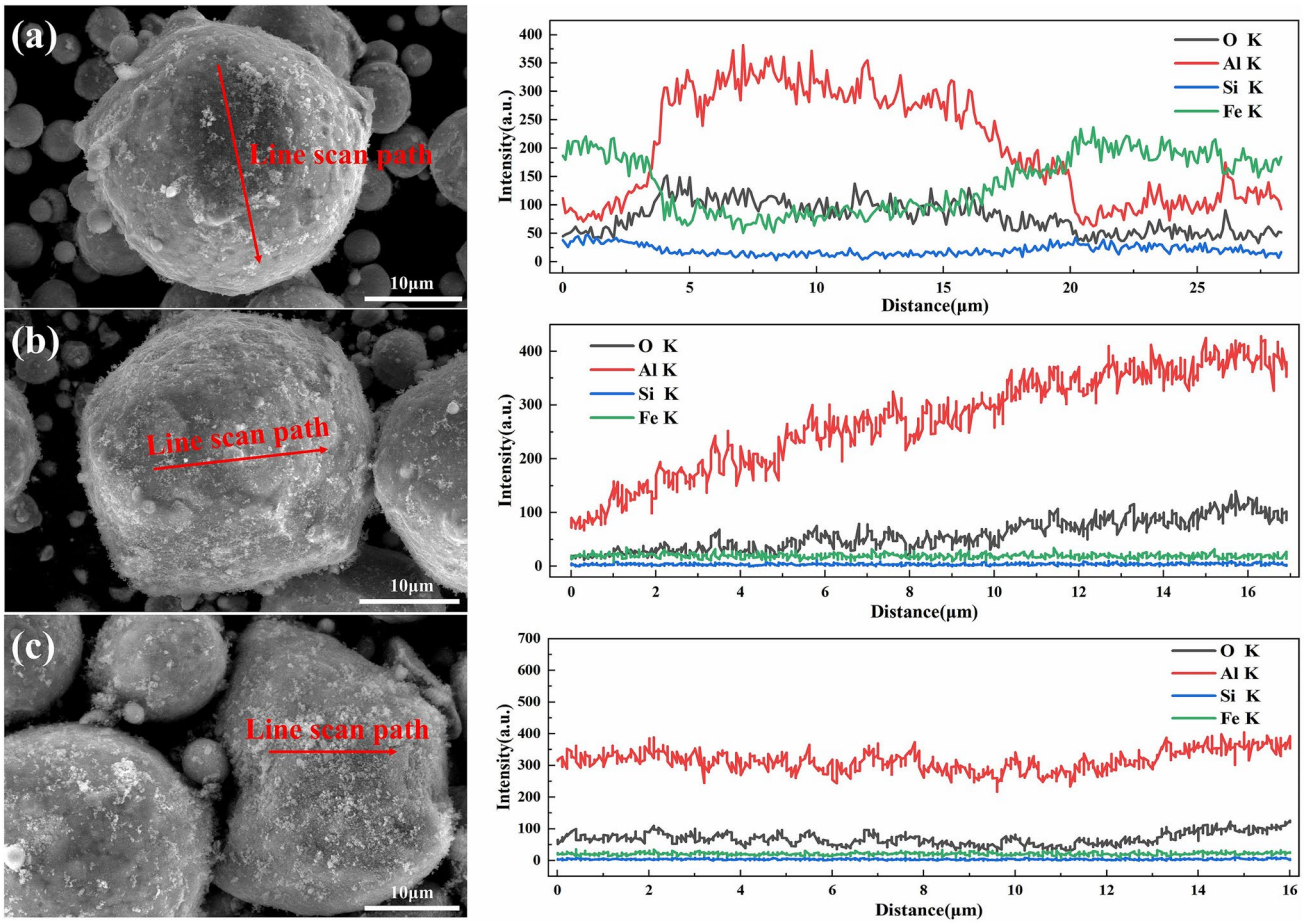


Fig. 3 EDS line scan profiles of Fe-Si powder with different coating contents: (a) 2.5 wt.%, (b) 5.0 wt.%, and (c) 7.5 wt.%.

mixed powders display additional diffraction peaks at 25.58° (012), 35.13° (104), 43.36° (113), 52.52° (116), and 68.20° (300), which are assigned to the α-Al_2O_3 phase. The appearance of these peaks confirms the presence of α-Al_2O_3 in the composite powders. Furthermore, no additional diffraction peaks attributable to other phases are detected, indicating that no impurities were introduced during the coating process.

Figure 2a–e shows the microstructures and corresponding magnified images of Fe-Si powders coated with different amounts of Al_2O_3. As the Al_2O_3 content increases from 0.0 wt.% to 10.0 wt.%, the Al_2O_3 content on the Fe-Si particle surfaces gradually increases. The uncoated Fe-Si powder (0.0 wt.%) exhibits a generally spherical morphology with uniformly distributed particles and smooth surfaces, and no obvious surface deposits are observed.

With increasing Al_2O_3 content, the surfaces of the Fe-Si powders become progressively covered by densely distributed fine particles, leading to a noticeably rougher and more irregular morphology. As the Al_2O_3 content increases from 2.5 wt.% to 7.5 wt.%, the surface coverage evolves from sparse and discontinuous deposits to a more continuous insulating layer. This progressive surface coverage is expected to enhance electrical insulation between adjacent Fe-Si particles after sintering, thereby suppressing the formation of interparticle eddy-current paths under high-frequency excitation.

To further analyze the evolution of the coating layer on the Fe-Si particle surfaces, EDS line-scan analysis was performed, as shown in Fig. 3a-c. For the powder containing 2.5 wt.% Al_2O_3, the Al signal is localized and fluctuates markedly along the examined path, indicating discontinuous local deposition. At 5.0 wt.%, the Al signal is distributed over a broader region and its average intensity increases, although local fluctuations remain. At 7.5 wt.%, the Al and O signals become comparatively stable along the examined path, while the Fe and Si signals are correspondingly weakened. The attenuation of Fe and Si signals, together with the elevated and more stable Al and O responses, is consistent with the formation of a relatively more continuous Al_2O_3-rich coating on the Fe-Si particle surface, which partially attenuates the signals from the inner Fe-Si substrate.

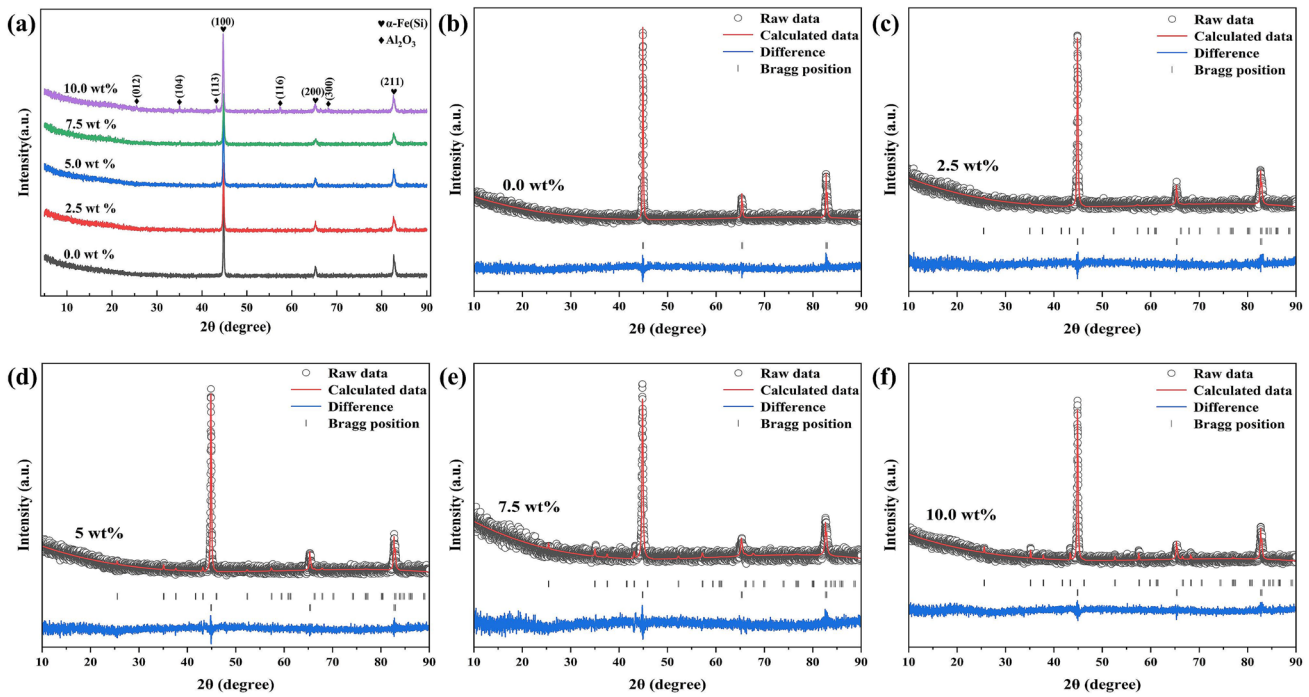


Fig. 4 (a) XRD patterns of SMCs with different Al_2O_3 coating contents. Rietveld refinement profiles of samples with Al_2O_3 contents of: (b) 0.0 wt.%, (c) 2.5 wt.%, (d) 5.0 wt.%, (e) 7.5 wt.%, and (f) 10.0 wt.%.

Table I Refined structural parameters and R_{wp} values of Fe(Si) and α-Al_2O_3 phases obtained from Rietveld refinement

Coating content	R_{wp} (%)	Phases	Lattice parameters						
			a (Å)	*b* (Å)	*c* (Å)	*V* (Å^3)	*α* (°)	*β* (°)	*γ* (°)
10.0 wt.%	8.2	α-Fe(Si)	2.8553	2.8553	2.8553	23.277	90	90	90
–	–	α-Al_2O_3	4.7578	4.7578	12.9888	254.633	90	90	120
7.5 wt.%	5.1	α-Fe(Si)	2.8579	2.8579	2.8579	23.343	90	90	90
–	–	α-Al_2O_3	4.7926	4.7926	13.0357	259.302	90	90	120
5.0 wt.%	5.4	α-Fe(Si)	2.8553	2.8553	2.8553	23.277	90	90	90
–	–	α-Al_2O_3	4.7834	4.7834	12.9953	257.51	90	90	120
2.5 wt.%	5.5	α-Fe(Si)	2.8557	2.8557	2.8557	23.289	90	90	90
–	–	α-Al_2O_3	4.7822	4.7822	13.0526	258.511	90	90	120
0.0 wt.%	4.5	α-Fe(Si)	2.8551	2.8551	2.8551	23.273	90	90	90
–	–	α-Al_2O_3	–	–	–	–	–	–	–

Figure 4a shows the XRD patterns of the SMCs with different Al_2O_3 contents. Rietveld refinement was performed on the XRD patterns, and the representative refinement profiles are shown in Fig. 4b–f. The calculated profiles agree well with the experimental data, while the difference curves exhibit only minor fluctuations. The obtained R_{wp} values range from 4.5% to 8.2% as shown in Table I, confirming the reliability of the refinement and indicating a satisfactory fitting quality. With increasing Al_2O_3 content, additional diffraction peaks corresponding to α-Al_2O_3 gradually appear and become more pronounced, indicating the successful retention of the insulating Al_2O_3 phase after SPS. Moreover, the SPS temperature employed in this study was 500°C, which is substantially lower than the temperatures generally reported for the formation of Fe-Al spinel phases and other reaction products in Fe/Al_2O_3 systems.[22,23] No secondary reaction products were detected within the detection limit of XRD, suggesting that the Al_2O_3 phase remains chemically stable during the SPS process and no obvious interfacial reaction occurs between Fe-Si and Al_2O_3.

Table II Phase fractions, space groups, and crystallite sizes of α-Fe(Si) and α-Al_2O_3 phases determined by Rietveld refinement.

Coating content	Phase	Space group	wt.%	Apparent crystallite size (nm)
10.0 wt.%	α-Fe(Si)	$Im\bar{3}m$	81.09	26.01
–	α-Al_2O_3	$R\bar{3}c$	18.91	57.80
7.5 wt.%	α-Fe(Si)	$Im\bar{3}m$	85.98	22.87
–	α-Al_2O_3	$R\bar{3}c$	14.02	44.90
5.0 wt.%	α-Fe(Si)	$Im\bar{3}m$	90.93	29.36
-	α-Al_2O_3	$R\bar{3}c$	9.07	48.43
2.5 wt.%	α-Fe(Si)	$Im\bar{3}m$	94.68	27.28
–	α-Al_2O_3	$R\bar{3}c$	5.32	68.45
0.0 wt.%	α-Fe(Si)	$Im\bar{3}m$	100	32.75

The refined structural parameters are summarized in Table I. The lattice parameter and unit-cell volume of the α-Fe(Si) phase show only marginal fluctuations with increasing Al_2O_3 content, indicating that the incorporation of Al_2O_3 has little influence on the crystal structure of the α-Fe(Si) matrix. This suggests that α-Al_2O_3 mainly exists as an independent insulating phase rather than dissolving into the α-Fe(Si) lattice. Therefore, no obvious lattice distortion or solid-solution effect is observed. Similarly, the lattice parameters of α-Al_2O_3 remain nearly unchanged, further confirming that the crystal structures of both phases are stable after SPS.

The phase fractions and crystallite sizes obtained from the Rietveld refinement are listed in Table II. As the nominal Al_2O_3 content increases, the refined α-Al_2O_3 fraction gradually increases from 5.32 wt.% to 18.91 wt.%, while the weight fraction of the α-Fe(Si) phase correspondingly declines from 94.68 wt.% to 81.09 wt.%. The refined α-Al_2O_3 fraction shows a monotonic increase with increasing nominal Al_2O_3 addition, confirming the retention of the Al_2O_3 phase after SPS.

In addition, the average crystallite size of the unmodified pure Fe-Si specimen is 32.75 nm, and it decreases to a range of 22.87–29.36 nm after Al_2O_3 is introduced. All Al_2O_3-containing composites have finer crystallites than the 0.0 wt.% sample. This observation reveals that the Al_2O_3 phase can effectively restrain crystallite coarsening during SPS.

Microstructure of the Fe-Si/Al_2O_3 SMCs

Figure 5a-e shows the backscattered electron images of the surfaces of Fe-Si/Al_2O_3 SMCs with different Al_2O_3 contents. For the sample without Al_2O_3 (0.0 wt.%), clearly defined particle boundaries are observed, together with a relatively dispersed pore distribution. With increasing Al_2O_3 content, more coating phase is introduced around the Fe-Si particles and becomes progressively distributed in the interparticle regions. The particle interfaces become less distinct due to the presence of the Al_2O_3-rich phase, indicating that the direct metallic contact between adjacent Fe-Si particles is gradually reduced. The coating is expected to suppress the formation of continuous eddy-current loops between Fe-Si particles under high-frequency excitation.

To further investigate the coating characteristics on the SMC surface, elemental mapping of O, Al, Si, and Fe was performed on the polished sample with 2.5 wt.% Al_2O_3.

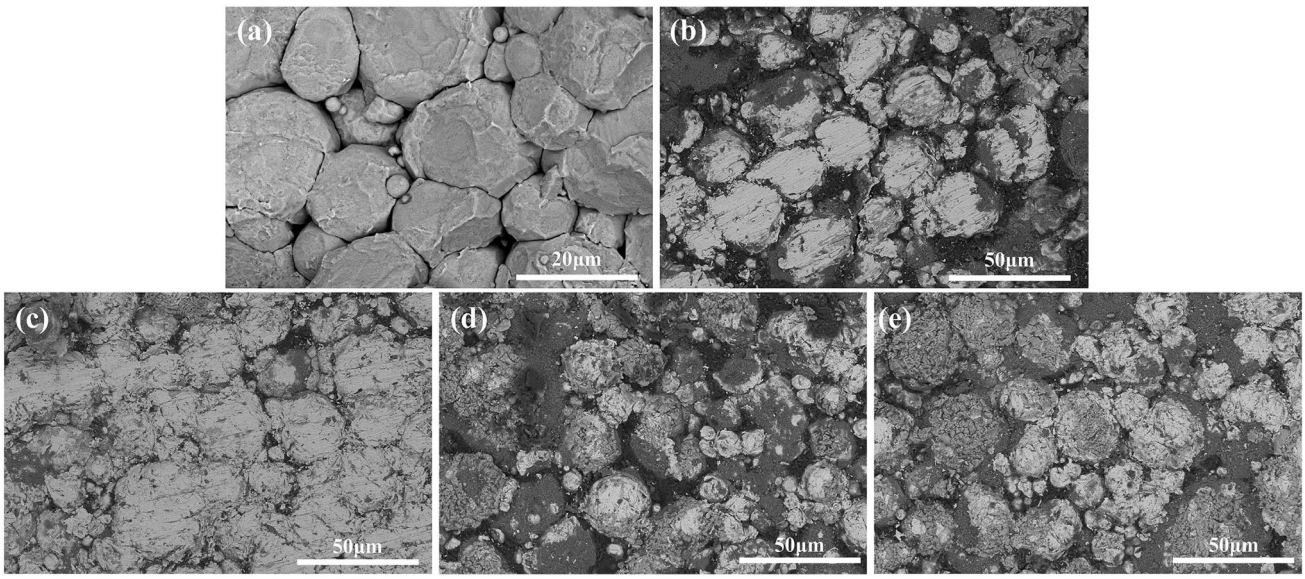


Fig. 5 Backscattered electron (BSE) images of Fe-Si SMCs surfaces with different Al_2O_3 contents: (a) 0.0 wt.%, (b) 2.5 wt.%, (c) 5.0 wt.%, (d) 7.5 wt.%, and (e) 10.0 wt.%.

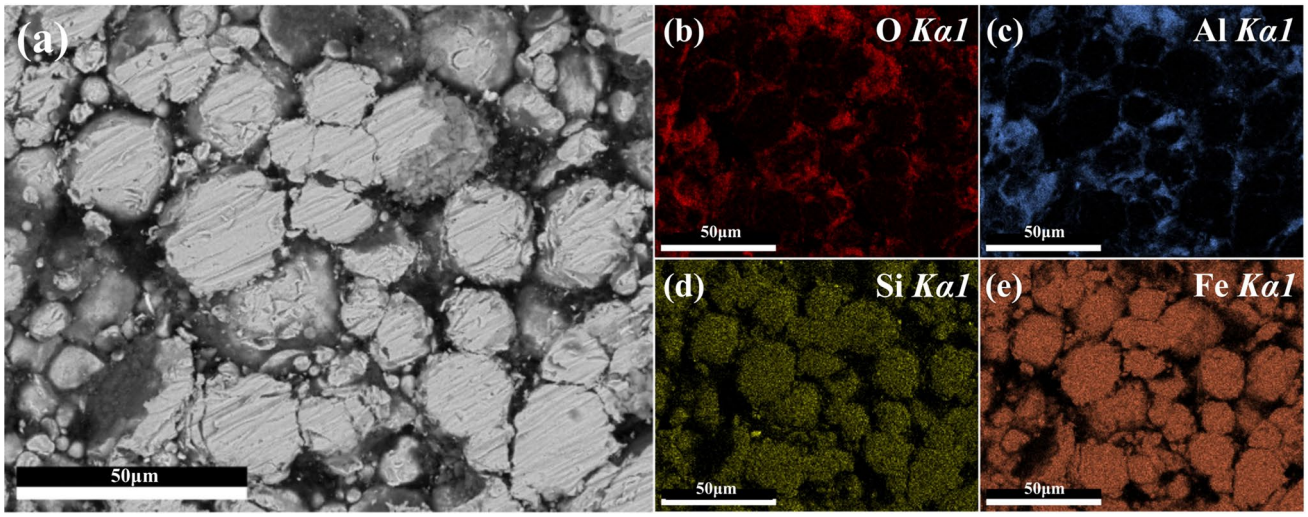


Fig. 6 (a) Backscattered SEM image of the polished SMC surface with 2.5 wt.% Al_2O_3 and corresponding EDS elemental maps for O, Al, Si, and Fe (b–e).

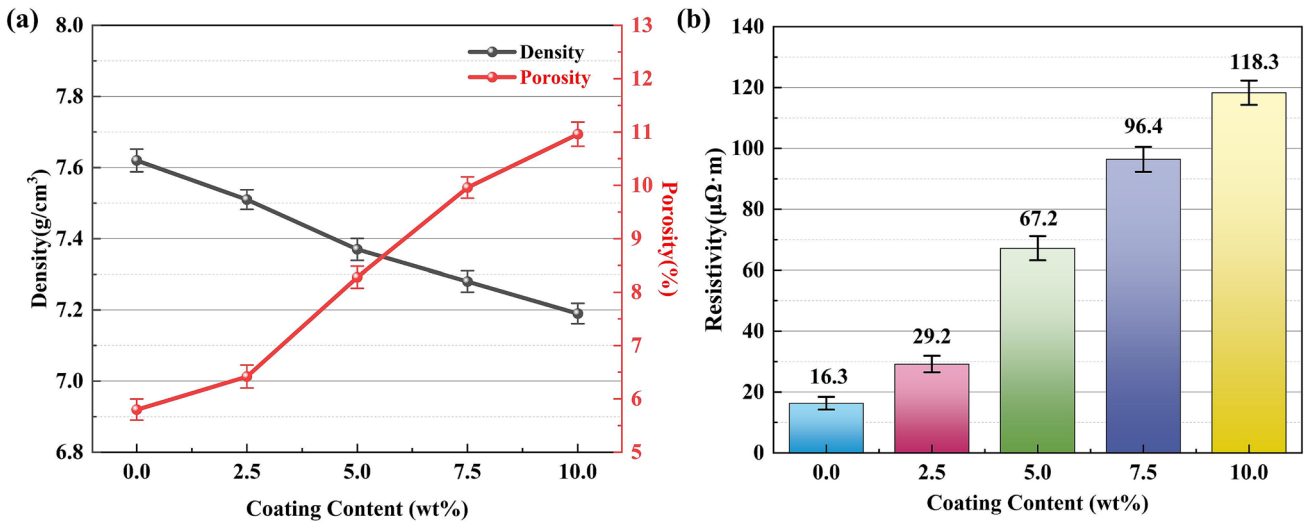


Fig. 7 (a) Density, porosity, and (b) resistivity of SMCs with different Al_2O_3 coating contents.

As shown in Fig. 6a, the quasi-spherical particles exhibit strong Si and Fe signals, confirming that they correspond to the Fe-Si matrix. In contrast, the interparticle regions show clear signals of Al and O, and the distribution of Al closely overlaps with that of O. This indicates that, after high-energy ball milling and subsequent SPS sintering, an Al_2O_3 coating layer is formed on the surface of the Fe-Si particles.

Physical Characteristics

Figure 7a presents the density and porosity of SMCs with five different Al_2O_3 coating contents. At a coating content of 0.0 wt.%, the SMC reaches its maximum density of 7.62 g/cm^3. As the coating content increases to 10.0 wt.%, the density decreases to 7.19 g/cm^3. This systematic reduction in density can be

attributed to the substantially lower density of Al_2O_3 compared with the Fe-Si alloy. As the proportion of Al_2O_3 increases, its volume fraction in the composite gradually becomes larger.

Correspondingly, the porosity increases with increasing Al_2O_3 content. This behavior indicates that the incorporation of Al_2O_3 hinders the densification process during SPS. As a high-melting-point ceramic phase, Al_2O_3 forms barrier layers between adjacent Fe-Si particles, reducing direct metallic contact. In addition, the introduction of Al_2O_3 alters the original packing arrangement of the powder particles, thereby weakening the localized current-assisted heating effect during SPS. Consequently, pore elimination becomes less effective, resulting in an increase in the residual porosity of the composites.

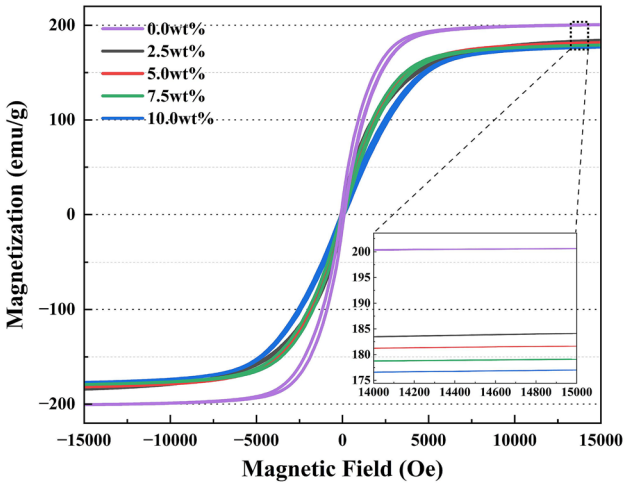


Fig. 8 Quasi-static hysteresis loops of SMCs with five different Al_2O_3 contents measured by VSM.

As illustrated in Fig. 7b, the electrical resistivity of the uncoated Fe-Si SMC is relatively low because direct electrical contact still exists between adjacent Fe-Si particles. With increasing Al_2O_3 content, more insulating phase is distributed around the Fe-Si particles, thereby enhancing the electrical insulation between adjacent particles and suppressing interparticle electron transport.[24]

It should be noted that the increase in electrical resistivity cannot be solely attributed to the insulating effect of the Al_2O_3 coating. With increasing Al_2O_3 content, the density of the composites gradually decreases, accompanied by a corresponding increase in porosity. The reduced densification during sintering introduces additional pores and interfacial defects, which interrupt conductive pathways and decrease the effective conductive cross-sectional area. Furthermore, the incorporation of Al_2O_3 refines the Fe-Si crystallites, resulting in a higher grain-boundary density and enhanced electron scattering. Therefore, the significant increase in electrical resistivity can be attributed to the combined effects of the continuous Al_2O_3 insulating network, increased porosity, reduced densification, and grain-boundary scattering.

According to the classical eddy-current loss theory, the eddy-current loss is inversely proportional to the electrical resistivity of the material. Therefore, the enhanced resistivity effectively suppresses interparticle eddy-current circulation and disrupts conductive current loops, resulting in a significant reduction in eddy-current loss.[25,26]

Magnetic Properties

Figure 8 shows the quasi-static hysteresis loops of the Fe-Si soft magnetic composites (SMCs) with different Al_2O_3

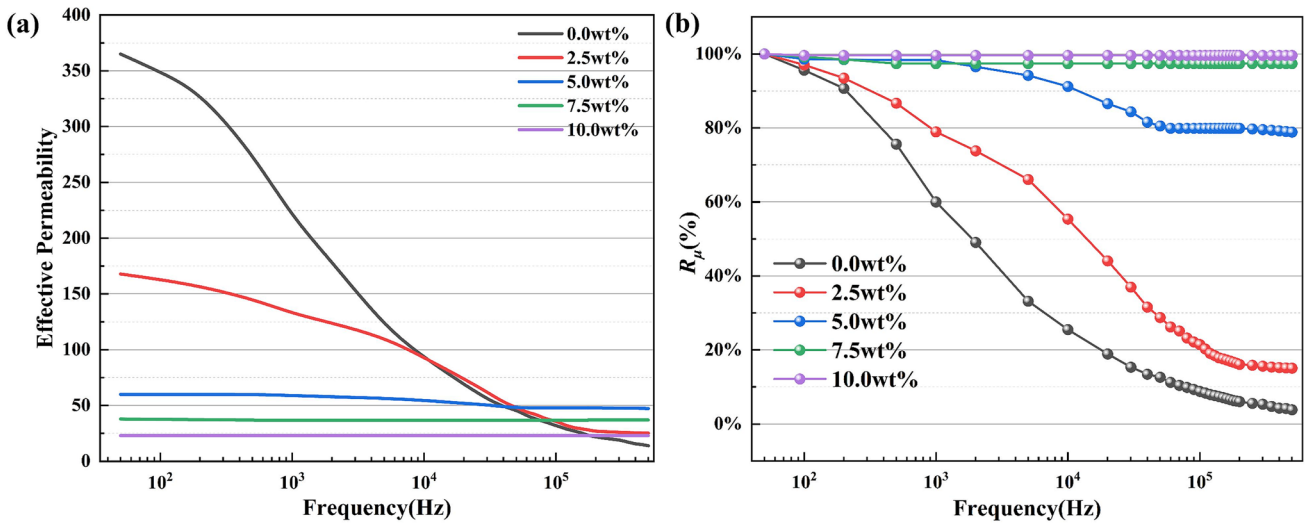


Fig. 9 (a) Frequency dependence of relative permeability for the five SMCs, (b) frequency stability (R_μ) below 500 kHz.

coating contents. As the Al_2O_3 content increases from 0.0 wt.% to 10.0 wt.%, the saturation magnetization (M_s) gradually decreases from 202.5 emu/g to 177 emu/g. Since M_s is primarily determined by the magnetic phase fraction and intrinsic magnetic properties of the material, the introduction of the nonmagnetic Al_2O_3 insulating phase inevitably reduces the relative content of ferromagnetic Fe-Si particles in the composites. Consequently, the number of magnetic atoms participating in magnetization per unit mass decreases, resulting in a progressive reduction in saturation magnetization. In addition, the presence of the insulating Al_2O_3 phase weakens the magnetic coupling between adjacent Fe-Si particles to some extent, which further contributes to the decline in the overall magnetic response of the composites.

As shown in Fig. 9a, the effective permeability of the Fe-Si/Al_2O_3 soft magnetic composites (SMCs) in the 10–500 kHz range exhibits a pronounced dependence on the Al_2O_3 content. With increasing Al_2O_3 addition, the maximum relative permeability shows an overall decreasing trend. This reduction is primarily attributed to the intrinsically nonmagnetic phase of Al_2O_3: a higher fraction of the nonmagnetic phase weakens the interparticle magnetic interactions among Fe-Si particles, thereby reducing the permeability of SMCs. In addition, the porosity rises gradually with the increase of Al_2O_3 content, introducing more nonmagnetic regions and breaking the continuity of magnetic flux paths. Meanwhile, the Al_2O_3 insulating layer isolates adjacent Fe-Si particles and weakens the interparticle magnetic coupling. The addition of Al_2O_3 refines Fe-Si crystallites and increases the quantity of grain boundaries; these abundant newly formed grain boundaries hinder domain-wall movement and further reduce magnetic coupling between neighboring particles. Moreover, residual stresses generated during SPS, especially those originating from the thermal expansion mismatch between Fe-Si and Al_2O_3, further impede domain-wall migration and magnetic moment rotation. The combined influence of all the above factors ultimately leads to the decline in magnetic permeability.[27–29]

$$R_\mu = \frac{\mu_e(f)}{\mu_e(f_0)} \times 100\% \quad (1)$$

To quantitatively compare the frequency stability of the effective permeability, the permeability retention ratio (R_μ) was introduced, as defined in Eq. 1. Here, $\mu_e(f)$ is the effective permeability at a given frequency, while $\mu_e(f_0)$ is the initial reference value measured at $f_0 = 50$ Hz. The uncoated sample exhibits a sharp decrease in R_μ with increasing frequency, indicating severe permeability degradation at high frequencies. With increasing Al_2O_3 content, the frequency stability of R_μ is progressively improved. In particular, the 5.0 wt.% Al_2O_3 sample retains about 80% of its initial permeability at high frequencies, while the 7.5 wt.% and 10.0 wt.% Al_2O_3 samples maintain nearly constant R_μ throughout the measured frequency range.

For SMCs, the skin effect generally causes a rapid reduction in the effective magnetic cross-sectional area with increasing frequency, leading to a decreased effective magnetized volume under high-frequency fields and, consequently, a pronounced permeability drop. The introduction of an Al_2O_3 insulating coating significantly suppresses interparticle eddy currents, thereby effectively mitigating the skin effect[30] and enabling the SMCs to retain a more stable permeability response over a broad high-frequency range.[31]

Loss Characteristics

The magnetic core loss P_{tot} represents the energy dissipated in soft magnetic composites (SMCs) under alternating electromagnetic excitation. As shown in Fig. 10a, P_{tot} decreases progressively with increasing Al_2O_3 content. When the Al_2O_3 content reaches 2.5 wt.% and 5.0 wt.%, P_{tot} decreases markedly compared with that of the unmodified sample, indicating that the incorporation of Al_2O_3 can effectively reduce the magnetic loss. At 500 kHz (20 mT), the P_{tot} of the SMCs with 5.0 wt.% Al_2O_3 decreased to 491.2 W/kg. When the Al_2O_3 content was increased to 10.0 wt.%, the loss further dropped to 88.1 W/kg, corresponding to an approximately 98.2% reduction compared with that of the 0.0 wt.% sample (5057.1 W/kg).

To quantitatively evaluate the contributions of different loss mechanisms under alternating magnetization, the Bertotti loss separation model was employed to decompose the total core loss into hysteresis loss, eddy-current loss, and excess loss.[32,33] The total loss can be expressed as follows:

$$P_{tot} = P_h + P_e + P_{exc} = C_h B_m^\alpha f + C_e B_m^2 f^2 + C_{exc} B_m^x f^y \quad (2)$$

where C_h, C_e, and C_{exc} are the fitting coefficients associated with the hysteresis loss P_h, eddy-current loss P_e, and excess loss P_{exc}, respectively. Physically, C_h reflects the intrinsic hysteresis-loss level related to irreversible domain-wall motion, magnetic anisotropy, and defect pinning during cyclic magnetization.[34] C_e characterizes the intensity of eddy-current dissipation and is closely related to the electrical resistivity, conductive path continuity, and effective eddy-current loop size in the SMCs. C_{exc} represents the contribution of dynamic excess loss, which is associated with nonuniform magnetization processes, localized eddy currents, and the motion of magnetically active domain structures under alternating magnetic fields. B_m represents the magnetic flux density, f denotes the frequency, while α, x, and y are fitting exponents describing the dependence of the

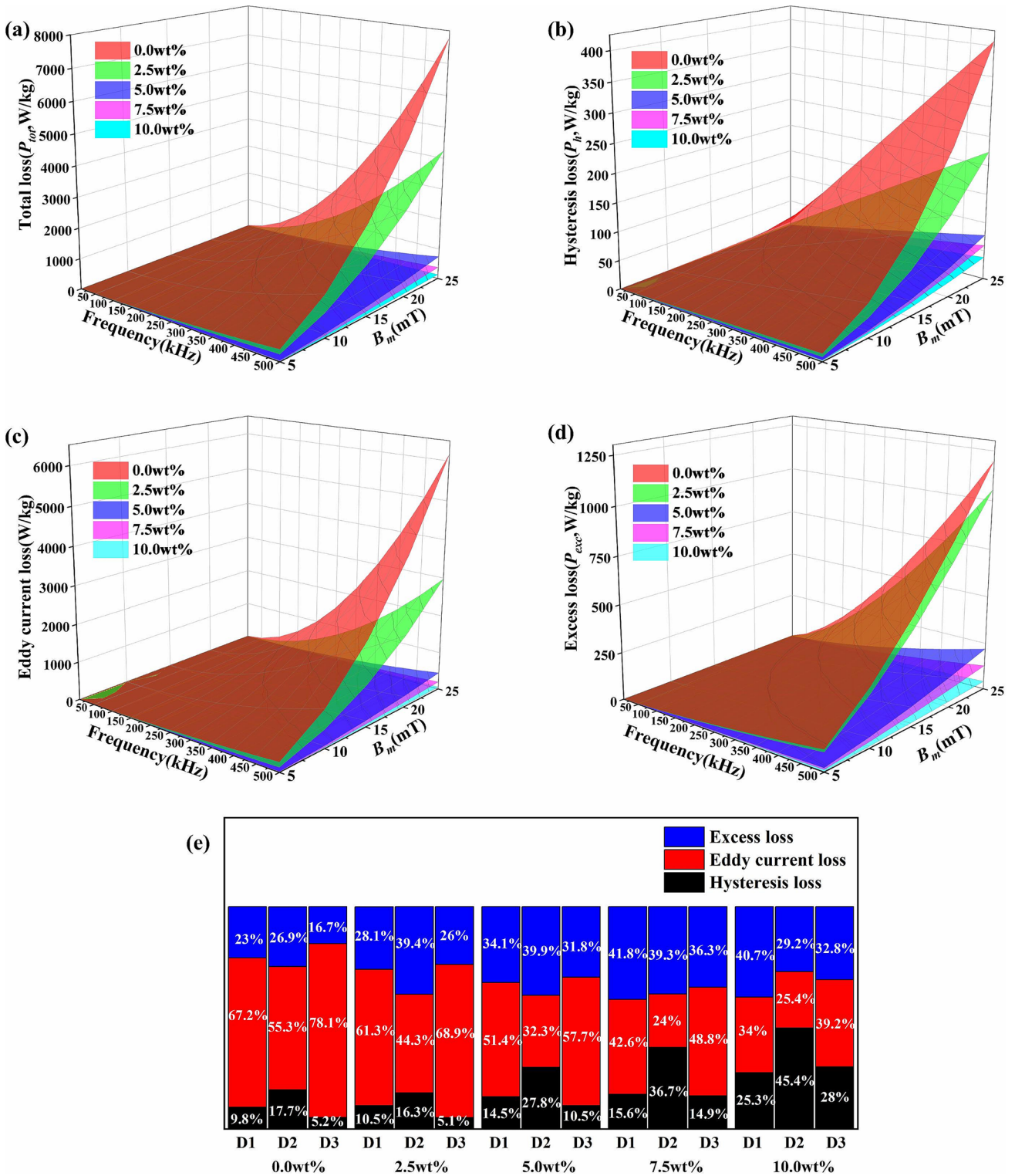


Fig. 10 Loss separation results of SMCs with different Al_2O_3 content under various frequencies and magnetic flux densities: (a) total core loss; (b) hysteresis loss; (c) eddy-current loss; (d) excess loss; and (e) relative contributions of hysteresis loss, eddy-current loss, and excess loss to the total core loss under selected operating conditions. D1: 10 mT, 500 kHz; D2: 20 mT, 100 kHz; D3: 20 mT, 500 kHz.

Table III Loss coefficients for Fe-Si/Al_2O_3 SMCs with different coating contents

Sample	C_h	α	C_{inter}	C_{intra}	C_{exc}	x	y
0.0 wt.%	2.27	2.13	8.46×10^{-7}	4.76×10^{-9}	8.60×10^{-4}	1.61	1.47
2.5 wt.%	1.03	2.18	4.05×10^{-7}	4.73×10^{-9}	7.55×10^{-4}	1.47	1.54
5.0 wt.%	0.29	2.05	5.64×10^{-8}	4.78×10^{-9}	1.57×10^{-4}	1.52	1.45
7.5 wt.%	0.19	2.01	2.18×10^{-8}	4.75×10^{-9}	9.13×10^{-5}	1.46	1.52
10.0 wt.%	0.11	1.98	8.41×10^{-9}	4.64×10^{-9}	2.91×10^{-5}	1.53	1.48

loss components on magnetic flux density and frequency. The relevant fitting parameters of Fe-Si SMCs with different Al_2O_3 coating contents are summarized in Table III.

Figure 10b–d presents the three-dimensional distributions of hysteresis loss, eddy-current loss, and excess loss as functions of B_m and f. The hysteresis loss decreases with increasing Al_2O_3 content. This behavior can be attributed to the enhanced interparticle insulation introduced by the Al_2O_3 phase, which weakens magnetic coupling between adjacent Fe-Si particles and suppresses irreversible domain-wall motion during magnetization.

Due to the discrete particle structure and the existence of interparticle conductive pathways in SMCs, the eddy-current loss (P_e) can be divided into intraparticle and interparticle components.[35,36] Therefore, P_e can be expressed as Eqs. 3 and 4:

$$P_e = P_e^{inter} + P_e^{intra} = \left(C_e^{inter} + C_e^{intra}\right)B_m^2 f^2 \tag{3}$$

$$C_e^{inter} = \frac{(\pi d_e)^2}{\beta \rho_0 r_0}, C_e^{intra} = \frac{(\pi d_s)^2}{20\rho_s r_s} \tag{4}$$

$$\beta = \frac{6}{1-0.633\frac{w}{h}\tanh\left(\frac{1.58h}{w}\right)} \tag{5}$$

where P_e^{inter} represents the eddy-current loss associated with macroscopic current loops formed through interparticle conductive networks, whereas P_e^{intra} corresponds to the eddy-current loss confined within individual Fe-Si particles. C_e^{inter} and C_e^{intra} are the corresponding eddy-current loss coefficients. Specifically, C_e^{inter} reflects the strength of interparticle eddy-current circulation and is governed by the effective eddy-current dimension d_e, the macroscopic electrical resistivity of the SMCs ρ_0, the geometry-related resistance factor r_0, and the geometrical correction factor β. β mainly depends on the difference between the outer and inner diameters. In Eq. 5, w and h denote the width and height of a single powder particle in the SMCs, respectively . In contrast, C_e^{intra} is mainly determined by the mean particle size d_s, the intrinsic electrical resistivity of Fe-Si particles ρ_s, and the particle-scale geometrical factor r_s. Since all samples were prepared using the same Fe-Si powders and identical SPS conditions, d_s, ρ_s, and r_s can be regarded as nearly unchanged. Therefore, the variation in eddy-current loss is mainly associated with the evolution of interparticle insulation, namely changes in ρ_0, r_0, and the continuity of conductive current paths.

As shown in Fig. 10c, the eddy-current loss decreases markedly with increasing Al_2O_3 content, especially under high-frequency and high-B_m conditions. This trend is quantitatively consistent with the fitted interparticle eddy-current coefficient. As listed in Table III, C_e^{inter} decreases from 8.46×10^{-7} for the uncoated sample to 8.41×10^{-9} for the samples containing 0.0 wt.% to 10.0 wt.% Al_2O_3, respectively. Meanwhile, the electrical resistivity increases from 16.3 to 118.3 μΩ m with increasing Al_2O_3 content. Since C_e^{inter} is inversely related to ρ_0, the increased resistivity directly contributes to the reduction in interparticle eddy-current loss.

The increase in bulk resistivity with increasing Al_2O_3 content is therefore an important factor responsible for the reduction in interparticle eddy-current loss. However, the bulk resistivity alone does not fully describe the insulation effectiveness of SMCs. In powder-based magnetic composites, an insulating phase may increase the apparent electrical resistivity even when it is locally aggregated or discontinuous. Combined with the SEM observations in Fig. 5, the Al_2O_3 phase becomes progressively more continuous and uniformly distributed around the Fe-Si particles as the coating content increases. The improved interfacial coverage reduces direct metallic contact between neighboring particles and shortens or interrupts the effective current loops under alternating magnetic fields.

This interpretation is supported by the coating evolution observed in the SEM and EDS results. At 2.5 wt.% Al_2O_3, the coating is relatively sparse and discontinuous, and some Fe-Si particles remain partially connected, resulting in only a moderate decrease in C_e^{inter}. When the Al_2O_3 content reaches 5.0 wt.%, the Al-containing phase becomes more widely distributed on the Fe-Si particle surfaces, leading to a sharp increase in resistivity and a pronounced reduction in C_e^{inter}. As the content further increases to 7.5 wt.% and 10.0 wt.%, the Al_2O_3 insulating phase becomes more continuous around the Fe-Si particles, thereby effectively blocking interparticle conductive channels and confining eddy currents within smaller local regions. Consequently, the interparticle eddy-current loss is substantially suppressed. In contrast,

Table IV Comparison of magnetic properties of representative Fe-based soft magnetic composites reported in recent studies

SMCs	Process	Coating content	Effective permeability	Core loss (W/kg)		M_s(emu/g)	Density (g/cm^3)
				20 mT	50 mT		
Fe-Si@Al_2O_3 (this work)	SPS	7.5 wt.%	37	20.7 at 100 kHz	547.5 at 100 kHz	179.1	7.28
Fe-Si@ZrO_2[40]	SPS	5.0 wt.%	–	–	968.0 at 100 kHz	174.93	–
FeSiAl@MnO/Al_2O_3[28]	SPS	5.0 wt.%	29.5	86.8 at 50 kHz	–	130.2	7.27
Fe@MnO_2[41]	SPS	5.0 wt.%	18.6	459.8 at 50 kHz	–	196.1	–
FeSiBCCr[42]	Cold pressing	–	22.97	–	–	153.2	6.212
FeSiBCCr@CIP[43]	Cold pressing	20.0 wt.%	30.9	–	–	140.2	5.45

C_e^{intra} remains within a relatively narrow range of 4.64×10^{-9} to 4.78×10^{-9}. This limited variation suggests that the intra-particle eddy-current response is only weakly affected by the Al_2O_3 content.

$$P_{exc} = 4I_{max}fH_{exc} = 8\sqrt{\sigma GSV_0}\left(I_{max}f\right)^{1.5} \quad (6)$$

As shown in Fig. 10d, the excess-loss surface gradually decreases with increasing Al_2O_3 content, particularly at high frequency and high magnetic flux density. P_{exc} can also be expressed by Eq. 6,[37,38] where I_{max} is the maximum magnetization, and H_{exc} is the excess magnetic field. Under high magnetization rates, σ denotes the effective electrical conductivity of the SMCs, G is a geometrical factor associated with the eddy-current path and is typically taken as 0.1356,[39] and S is the effective cross-sectional area perpendicular to the magnetic flux. V_0 is a phenomenological parameter associated with the magnetically active objects participating in dynamic magnetization and is treated as a fitting-related quantity in the excess-loss analysis.

According to the above relationship, the excess-loss-related contribution is closely related to the effective electrical conductivity of the SMCs. With increasing Al_2O_3 content, the high-resistivity insulating phase progressively interrupts interparticle electron transport and reduces the effective electrical conductivity of SMCs. Consequently, the localized eddy-current dissipation associated with non-uniform dynamic magnetization is weakened. Moreover, the more continuous and homogeneous Al_2O_3 distribution around the Fe-Si particles, as observed in Fig. 5, reduces direct metallic contact between adjacent particles and mitigates local current concentration at particle interfaces. These effects improve the local electromagnetic uniformity under high-frequency excitation and further suppress the excess-loss-related contribution.

As shown in Fig. 10e, the relative contributions of the different loss components vary markedly with the Al_2O_3 content. For the uncoated Fe-Si SMC, eddy-current loss accounts for a large proportion of the total loss, particularly under high-frequency conditions, especially at 500 kHz. After introducing the Al_2O_3 insulating phase, the relative contribution of eddy-current loss decreases significantly, whereas the proportions of hysteresis loss and excess loss increase to some extent. The analysis of the relative loss contributions further confirms that the Al_2O_3 insulating phase can effectively interrupt interparticle conductive pathways, thereby reducing eddy-current loss.

To further evaluate the performance of the present Fe-Si/Al_2O_3 SMCs, a comparison with previously reported SMCs is summarized in Table IV. Compared with previously reported SPS-processed Fe-based SMCs employing different insulating phases, the present Fe-Si/Al_2O_3 composites exhibit significantly lower core loss under comparable testing conditions while maintaining favorable magnetic properties. In particular, the sample containing 7.5 wt.% Al_2O_3 achieves a total core loss of only 20.7 W/kg at 100 kHz and 20 mT. Furthermore, compared with conventionally cold-pressed SMCs, the SPS-fabricated composites exhibit higher density and improved magnetic performance, which can be attributed to the enhanced densification and interparticle bonding achieved during SPS. These results demonstrate that the combination of Al_2O_3 interparticle insulation and SPS processing is highly effective for developing high-frequency soft magnetic composites.

Conclusions

In this study, Fe−6.5 wt.% Si/Al_2O_3 soft magnetic composites were successfully fabricated by high-energy ball milling followed by SPS. The effects of Al_2O_3 content on the microstructure, electrical resistivity, permeability, and core-loss behavior were systematically investigated. With increasing Al_2O_3 content, the insulating layer on the Fe-Si particle surfaces gradually evolved from discontinuous coverage (2.5 wt.%) to a more continuous and homogeneous structure (7.5 wt.%), leading to enhanced interparticle insulation and increased electrical resistivity. As a result, the high-frequency permeability stability was significantly improved, and the total core loss was greatly reduced. At

500 kHz and 20 mT, the total loss decreased from 5057.1 W/kg for the uncoated sample to 491.2 W/kg for the 5.0 wt.% SMC and further to 88.1 W/kg for the 10.0 wt.% SMC. Loss separation analysis further confirmed that the reduction in core loss was mainly attributed to the suppression of interparticle eddy-current loss. However, excessive Al_2O_3 introduced more nonmagnetic phase and weakened magnetic coupling between Fe-Si particles, leading to reduced permeability. The SMC containing 7.5 wt.% Al_2O_3 exhibited the best comprehensive magnetic performance, with an effective permeability of 37 and a core loss of 253.611 W/kg at 500 kHz and 20 mT. This work provides a useful approach for optimizing Fe-Si-based SMCs for high-frequency electromagnetic applications.

Acknowledgments This work was supported in part by the National Natural Science Foundation of China, (No. 52277008).

Author Contributions Fugui Liu conceptualized the study, acquired funding, and reviewed and edited the manuscript. Yupeng Chen performed the methodology development, data curation, validation, and original draft writing. Changgeng Zhang contributed to manuscript review and editing, provided resources, and was responsible for project administration and funding acquisition. Zhiwei Lin supervised the work and contributed to methodology development, formal analysis, resource provision, and project administration. Yongjian Li provided resources and contributed to project administration and funding acquisition. Kai Liu performed data curation.

Conflict of interest The authors declare that they have no known competing financial interests or personal relationships that could have appeared to influence the work reported in this paper.

References

1. K.J. Sunday and M.L. Taheri, Soft magnetic composites: Recent advancements in the technology. *Met. Powder Rep*. 72, 425 (2017).
2. J. Liu, L. Zhang, and H. Wu, Electromagnetic wave-absorbing performance of carbons, carbides, oxides, ferrites and sulfides: review and perspective. *J. Phys. D Appl. Phys.* 54, 373002 (2021).
3. A. Talaat, M.V. Suraj, K. Byerly, A. Wang, Y. Wang, J.K. Lee, and P.R. Ohodnicki, Review on soft magnetic metal and inorganic oxide nanocomposites for power applications. *J. Alloys Compd.* 870, 159500 (2021).
4. C. Zhang, B. Jiang, Y. Li, and Q. Yang, Magnetic measurement of soft magnetic composites material under 3D SVPWM excitation. *AIP Adv.* 8, 056028 (2018).
5. B. Santhi, D.A. Babu, and U.M.R. Seelam, Mechanical and magnetic properties of phase separated Cu50Fe50 (at.%) alloys synthesized by mechanical alloying and spark plasma sintering. *J. Alloys Compd.* 997, 174890 (2024).
6. J.M. Silveyra, E. Ferrara, D.L. Huber, T.C. Monson, Soft magnetic materials for a sustainable and electrified world. Science 362. eaao0195 (2018)
7. X. Yu, Y. Li, Q. Yang, S. Yue, and C. Zhang, Loss characteristics and model verification of soft magnetic composites under non-sinusoidal excitation. *IEEE Trans. Magn.* 55, 8401204 (2019).
8. S. Wu, A.Z. Sun, F.Q. Zhai, J. Wang, Q. Zhang, W.H. Xu, P. Logan, and A.A. Volinsky, Annealing effects on magnetic properties of silicone-coated iron-based soft magnetic composites. *J. Magn. Magn. Mater.* 324, 818 (2012).
9. C. Bolfarini, M.C.A. Silva, A.M. Jorge, C.S. Kiminami, and W.J. Botta, Magnetic properties of spray-formed Fe-6.5%Si and Fe-6.5%Si-1.0%Al after rolling and heat treatment. *J. Magn. Magn. Mater.* 320, 653 (2008).
10. R. Wang, X. Liao, L. Kang, H. Kong, Z. Wu, and H. Wang, Evolution of insulating layers during heat treatment and their effects on magnetic behavior of Fe-Si-Al based soft magnetic composites. *Ceram. Int.* 49, 17876 (2023).
11. D. Liu, C. Wu, M. Yan, and J. Wang, Correlating the microstructure, growth mechanism and magnetic properties of FeSiAl soft magnetic composites fabricated via HNO_3 oxidation. *Acta Mater.* 146, 294 (2018).
12. M.Q. Huang, C. Wu, Y.Z. Jiang, and M. Yan, Evolution of phosphate coatings during high-temperature annealing and its influence on the Fe and FeSiAl soft magnetic composites. *J. Alloys Compd.* 644, 124 (2015).
13. A.H. Taghvaei, H. Shokrollahi, K. Janghorban, and H. Abiri, Eddy current and total power loss separation in the iron-phosphate-polyepoxy soft magnetic composites. *Mater. Des.* 30, 3989 (2009).
14. I. Hemmati, H.R. Madaah, and A. Kianvash, The correlations between processing parameters and magnetic properties of an iron-resin soft magnetic composites. *J. Magn. Magn. Mater.* 305, 147 (2006).
15. C. Zhang, Z. Guo, Z. Lin, and Y. Li, High performance soft magnetic composites based on Fe/Ni-Zn ferrite powder prepared by low-pressure spark plasma sintering. *J. Alloys Compd.* 1012, 178436 (2025).
16. W. Li, H. Cai, Y. Kang, X. Yu, J. Zheng, Y. Qiao, and S. Che, High permeability and low loss bioinspired soft magnetic composites with nacre-like structure for high frequency applications. *Acta Mater.* 167, 267 (2019).
17. J. Zheng, H. Zheng, J. Lei, Y. Qiao, W. Li, and X. Yu, Magnetic properties and microstructure of iron-based soft magnetic composites with Al_2O_3 insulating coating by one-pot synthesis method. *J. Magn. Magn. Mater.* 499, 166259 (2020).
18. M. Yaghtin, A.H. Taghvaei, B. Hashemi, M. Janghorban, and H. Shokrollahi, Effect of heat treatment on magnetic properties of iron-based soft magnetic composites with Al_2O_3 insulation coating produced by sol-gel method. *J. Alloys Compd.* 581, 293 (2013).
19. S. Lu, M. Wang, and Z. Zhao, Recent advances and future developments in Fe-based amorphous soft magnetic composites. *J. Non-Cryst. Solids* 616, 122440 (2023).
20. J.L. Grosseau-Poussard, X. Milhet, C. Huvier, and J.F. Dinhut, Consolidation of iron powders through the influence of phosphate thin films. *J. Mater. Process. Technol.* 205, 151 (2008).
21. S. Saberi, M. Stockinger, C. Stoeckl, B. Buchmayr, H. Weiss, R. Afsharnia, and K. Hartl, A new development of four-point method to measure the electrical resistivity in situ during plastic deformation. *Measurement* 180, 109547 (2021).
22. K. Zhang, Y. Li, H. Yan, C. Wang, H. Li, J. Liang, and J. Dang, Effect of sintering temperature on microstructure and mechanical properties of hot-pressed Fe/$FeAl_2O_4$ composite. *Crystals* 11, 422 (2021).
23. J. Gurt Santanach, C. Estournès, A. Weibel, A. Peigney, G. Chevallier, and C. Laurent, Spark plasma sintering as a reactive sintering tool for the preparation of surface-tailored Fe-$FeAl_2O_4$-Al_2O_3 nanocomposites. *Scripta Mater.* 60, 195 (2009).
24. P. Wang, Z. Zhu, J. Liu, H. Zhao, J. Pang, and J. Zhang, Soft magnetic properties regulation of FeSiBC amorphous powders/CIP magnetic powder core with single and double-layer core-shell structure. *J. Magn. Magn. Mater.* 578, 170809 (2023).
25. A.F. Mayadas and M. Shatzkes, Electrical-resistivity model for polycrystalline films: the case of arbitrary reflection at external surfaces. *Phys. Rev. B* 1, 1382 (1970).
26. C.T. Yang, Y.F. Huang, C.W. Tien, K.Y. Wu, H.S. Huang, and H.I. Hsiang, FeSiCr–RIP/CIP soft magnetic composites: microstructure

(EBSD–KAM), core loss, and DC-bias for molded inductors. *J. Sci. Mater. Elec.* 37(7), 520 (2026).
27. H. Li, G. Bai, R. Zhao, H. Yang, Z. Lu, M. Cheng, R. Su, S. Bandaru, Y. Zhang, X. Liu, Z. Li, E. Zhang, Z. Zhang, M. Zhang, X. Liu, and X. Zhang, High-performance FeSiAl soft magnetic composites achieved by confined solid-state reaction. *Acta Mater.* 255, 119102 (2023).
28. F. Luo, X.A. Fan, Z. Luo, W. Hu, J. Wang, Z. Wu, and Y. Li, Preparation and magnetic properties of FeSiAl-based soft magnetic composites with MnO/Al_2O_3 insulation layer. *J. Magn. Magn. Mater.* 498, 166084 (2020).
29. J. Lai, L. Xiao, Z. Xiong, L. Fang, W. Zhu, F. Kuang, and Z. Gao, Enhanced soft magnetic properties and high-frequency stability of FeNiMo powder cores by coating SiO_2 insulation layer. *RSC Adv.* 13, 15892 (2023).
30. M.C. Kulan, N.J. Baker, K.A. Liogas, and A. Kladas, Empirical implementation of the Steinmetz equation to compute eddy-current loss in soft magnetic composite components. *IEEE Access* 10, 14610 (2022).
31. B. Zhou, Y. Dong, Q. Chi, P. Wang, and H. Zhao, Fe-based amorphous soft magnetic composites with SiO_2 insulation coatings: a study on coating thickness, microstructure and magnetic properties. *Ceram. Int.* 46, 13449 (2020).
32. R. Wang, H. Huang, H. Kong, A. Xia, L. Zhou, Z. Wu, and X. Gao, FeSi@BN soft magnetic composites inspired by fried glutinous rice balls: a core–shell design for enhanced magnetic and thermal performance in high-frequency power applications. *Chem. Eng. J.* 515, 163501 (2025).
33. R. Wang, X. Zhao, X. Li, H. Kong, Z. Sun, A. Xia, Z. Wu, Gradient nanostructure, diffusion mechanisms, and performance of Fe-Si (6.5 wt.%) alloy powders prepared using a green and controllable method. Small Methods 10. e70677 (2026)
34. G.K. Shi, Y. Wang, J. Li, and X. Zhao, Effect of particle size on eddy-current loss of soft magnetic composites using combined DEM and FEM. *IEEE Trans. Magn.* 60, 2000708 (2024).
35. X. Zhao, X. Liu, H. Zhao, Y. Wang, Two-dimensional vector hysteresis modeling for soft magnetic composite materials considering anisotropic property. In: 2020 IEEE Industry Applications Society Annual Meeting (IEEE, Piscataway, NJ, 2020). 1–6
36. O.D. Barrière, C. Appino, F. Fiorillo, C. Ragusa, and M. LoBue, Characterization and prediction of magnetic losses in soft magnetic composites under distorted induction waveforms. *IEEE Trans. Magn.* 49(3), 1318 (2013).
37. S. Lu, T. Liu, M. Wang, Z. Zhao, (2025) Effect of adding MgO underlayer on interface behavior and magnetic performance of Fe-6.5Si/(ZnNi)Fe2O4 composite prepared by spark plasma sintering. J. Alloys Compd. 1016. 178874
38. G. Bertotti, General properties of power losses in soft ferromagnetic materials. *IEEE Trans. Magn.* 24(1), 621 (1988).
39. A.P.S. Baghel and S.V. Kulkarni, Dynamic loss inclusion in the Jiles-Atherton hysteresis model using the original JA approach and the field separation approach. *IEEE Trans. Magn.* 50, 7300209 (2014).
40. K. Geng, Y. Xie, L. Yan, and B. Yan, Fe-Si/ZrO_2 composites with core-shell structure and excellent magnetic properties prepared by mechanical milling and spark plasma sintering. *J. Alloys Compd.* 718, 53 (2017).
41. Y. Zhang, X.A. Fan, W. Hu, J. Wang, Z. Wu, Y. Li, and X. Liu, Microstructure and magnetic properties of MnO_2 coated iron soft magnetic composites prepared by ball milling. *J. Magn. Magn. Mater.* 514, 167295 (2020).
42. J. Shen, B. Wang, L. Liu, L. Cai, B. Wang, Y. Yu, Y. Tian, J. Dong, and G. Wang, Magnetic properties of high DC bias performance Fe-Si-B-C-Cr amorphous soft magnetic composites. *ACS Appl. Electron. Mater.* 5, 4462 (2023).
43. J. Liu, Y. Dong, P. Wang, Z. Zhu, H. Zhao, J. Pang, and J. Zhang, Improved high-frequency magnetic properties of FeSiBCCr amorphous soft magnetic composites by adding carbonyl iron powders. *J. Non-Cryst. Solids* 605, 122166 (2023).

Publisher's Note Springer Nature remains neutral with regard to jurisdictional claims in published maps and institutional affiliations.

Springer Nature or its licensor (e.g. a society or other partner) holds exclusive rights to this article under a publishing agreement with the author(s) or other rightsholder(s); author self-archiving of the accepted manuscript version of this article is solely governed by the terms of such publishing agreement and applicable law.

Authors and Affiliations

Fugui Liu[1] · Yupeng Chen[1] · Changgeng Zhang[1] · Zhiwei Lin[1,2] · Yongjian Li[1] · Kai Liu[1]

✉ Changgeng Zhang
changgeng.zhang@hebut.edu.cn

[1] State Key Laboratory of Intelligent Power Distribution Equipment and System, Hebei University of Technology, Tianjin 300401, People's Republic of China

[2] Ningbo Magnetic Materials Application Technology Innovation Center Co., Ltd, Ningbo 315100, Zhejiang, People's Republic of China